RESEARCH ARTICLE

Influence of an Increasing Alloying Content on the Microstructure of a High-Speed Steel in the Laser-Powder Bed Fusion Process

Johannes Kunz, Marie Luise Köhler,* Simone Herzog, Anke Kaletsch, and Christoph Broeckmann

Tool steels being processed by laser powder bed fusion (LPBF) receive increasing attention in research. High hardness and low toughness lead to a challenging crack susceptibility of these alloys. Latest advancements in process technology have shown promising results toward crack-free build-up of additive manufactured tools. Detailed microstructure analysis is carried out to understand the mechanisms of solidification as an influencing factor for cracking. These findings can provide insights toward an alloy optimization regarding a higher intrinsic crack resistance while maintaining the typical mechanical properties of tool steels. PMHS 6–5–3–8 high-speed steel shows directional dendritic solidification with carbides mainly precipitating in enriched interdendritic areas. Increasing the alloying content by additions of PMHS 7–7–7–11 leads to a shift toward a less-pronounced texture. The positive effect of texture reduction is superimposed by a highly increased crack formation due to carbide networks.

1. Introduction

One of the most common procedures for additive manufacturing of metals is laser powder bed fusion (LPBF). Based on CAD data, a laser melts the desired structure layerwise in a powder bed.[1]

In recent years, the investigation of the mechanical properties of steels has concentrated on a few steel grades, e.g., H13, AISI316L, 17-4PH, and 15-5 PH.[2] The effect of the LPBF process on steels with higher carbon contents, e.g., cold-work and high-speed steels, has hardly been investigated.

High carbon steels show a tendency for cold crack formation during LPBF processing. These cold cracks are attributed to large

J. Kunz, M. L. Köhler, S. Herzog, A. Kaletsch, C. Broeckmann
Institute for Materials Applications in Mechanical Engineering
RWTH Aachen University
Augustinerbach 4, Aachen 52062, Germany
E-mail: m.koehler@iwm.rwth-aachen.de

The ORCID identification number(s) for the author(s) of this article can be found under https://doi.org/10.1002/srin.202100438.

residual stresses from the high temperature gradients and complex thermal profiles within the built-up structure.[3] Coarse eutectic carbide networks have been identified as crack initiators in cast high alloy tool steels leading to the processing of tool steels containing 3% of V in the powder metallurgical form where carbides are finely dispersed.[4] A lot of research is carried out to modify process setting toward crack–free production of high alloyed steels by LPBF.[3,5] A new tool steel alloy has been developed and analyzed regarding LPBF processability and mechanical properties by Sander et al.[6] and Kochta et al.[7] Understanding the crack initiating factors in the microstructure of LPBF tool steel and process parameter influenced microstructure tailoring for fine dispersion of carbides can deliver a valuable input for alloy design of tailored LPBF materials.

Processing powder mixtures by additive manufacturing have become a route for researchers to evaluate the influence of the alloys' composition. Powders with similar properties, such as particle size distribution, density, and morphology have been proven to be processable to a chemically homogeneous microstructure.[8]

High cooling rates in LPBF and limited diffusion activity lead to a nonequilibrium microstructure and the formation of metastable phases.[2] In addition, constitutional supercooling becomes relevant for the solidification of highly alloyed materials. Due to solid solution limits of the solidifying phase, the residual melt is enriched in alloying elements. With increasing concentrations of alloying elements in the melt, the liquidus temperature of the melt decreases. This phenomenon is known as constitutional supercooling. With increased supercooling, a shift from columnar dendritic solidification toward equiaxed dendritic solidification is expected.[9]

Research carried out by Kwok et al.[10] on laser melted PMHS 6–5–3–8 showed columnar dendritic solidification with martensite being the dominant phase in the dendrite center. Carbides surrounded by retained austenite are observed in the interdendritic regions. A study by Geenen et al.[11] revealed Mo, V, and W enriched areas in the intercellular space in the microstructure attributing them to solidification segregation. During postprocessing heat treatments, carbides form preferred in these areas. Lee et al.[12] observed plate-shaped M_2C carbides (M—metallic element, C—carbon) which form a discontinuous network whereas fine, spherical MC carbides are uniformly distributed in the matrix

material. Regions enriched in carbide forming elements have also been reported to stabilize retained austenite in AISI M50 steel in a study of Tang et al.[13] Detailed carbide analysis in several cast high-speed steels by Hwang et al.[14] show that W and Mo additions lead to the formation of needle-like M_2C and M_6C carbides in the intercellular region. With increasing V contents in the range of 3.6–5% they observed a shift from MC carbides mainly precipitating on cell boundaries towards precipitation inside the cells.

Based on PMHS 6–5–3–8 the composition of the steels that are subject of this study have been modified by additions of PMHS 7–7–7–11 to the feedstock. The aim was the investigation of the effect of the compositional change on the microstructure. Experiments with the powder mixtures of the alloys allow an investigation of the effects of an increase in carbide forming elements on the processability and solidification morphology.

2. Experimental Section

2.1. Material

The high-speed steel powder of PMHS 6–5–3–8 (DIN No. 1.3294[15]) and PMHS 7–7–7–11 (DIN No. 1.3292[15]) used in this study was manufactured in a nitrogen gas atomization process by Deutsche Edelstahlwerke (Krefeld, Germany). Both powders were provided in a particle size distribution of 15–53 μm. They were processed by LPBF in their pure form and as mixed feedstock in the mass ratios 70:30, 50:50, and 30:70. The morphology and the chemical composition of the powder are shown in **Figure 1** and **Table 1**. Table 1 shows the calculated theoretical composition of the three powder mixtures included. PMHS 6–5–3–8 (Figure 1a) shows more particles with a rough surface area. PMHS 7–7–7–11 (Figure 1b) shows a smooth particle surface with few satellites covering the powder particles. The apparent densities of the powders were determined to be 4.2 g cm^{-3} for PMHS 6–5–3–8 and 4.3 g cm^{-3} for PMHS 7–7–7–11 according to DIN ISO 3923-1.[16]

The feedstocks were mixed for 30 min in a tumble mixer immediately before being processed by LPBF.

2.2. Thermodynamic Calculations

Thermodynamic calculations provided valuable information for the interpretation of the microstructures formed in the experiments. They were carried out with Thermo-Calc software[17] and the TCFE9 database on the chemical compositions of the used alloys. Equilibrium calculations were used to determine the effect of the change in chemical composition on the stabilized phases.

Scheil–Gulliver calculations were used to predict the solidification induced segregation, which is expected to occur caused by high cooling rates during LPBF. Starting from the liquidus temperature, calculations were carried out in 0.5 K steps until a residual melt fraction of 3 wt% was reached. Carbon was considered as a back-diffusing interstitial element in the calculation.

2.3. LPBF Process

The LPBF process was carried out on a Realizer SLM 100 machine. The machine is equipped with a pulsating ytterbium fiber laser (1070 ± 2.5 nm) with a maximum power of 200 W. Twelve cubic specimen (10 × 10 × 10 mm^3) (**Figure 2**a) within a predefined window of process parameters were built up from each alloy. The arrangement of the specimens is shown in Figure 2b.

Used parameter sets are shown in **Table 2**. The exposure point distance and exposure time, which results in the scanning speed v, were varied. Laser power P of 160 W, hatch distance h of 0.1 mm, and layer thickness d of 30 μm were kept constant. The energy density E_v, shown in Equation (1), is used to describe the irradiated laser energy in a specific volume element. The building plate preheating temperature was set to 500 °C.

$$E_V = \frac{P}{h \cdot v \cdot d} \tag{1}$$

A stripe scanning strategy (Figure 2c) with a width of 2.7 mm was applied, leading to an overlap of 0.1 mm to the sides of each stripe. Within the stripes, the exposure was carried out in a zig–zag pattern. The hatch direction was rotated by 90° after each layer.

Argon was used as process gas. Cooling from the process temperature to 60 °C takes approximately 60 min and is not controlled in terms of temperature. The process chamber is constantly kept under argon atmosphere during the cooling.

2.4. Microstructural Analysis

In-depth microstructure analysis was carried out for PMHS 6–5–3–8, the 50:50 alloy, and PMHS 7–7–7–11. For simplicity reasons, results of microstructural analyses for the 70:30 and 30:70 alloys are excluded. For microstructural analysis, the cubes were cut vertically, the surface was ground and polished. Light optical microscopy (LOM) on unetched specimens was used to determine the relative density by means of image analysis. Five grayscale images (100× magnification) of the cross section with a resolution of
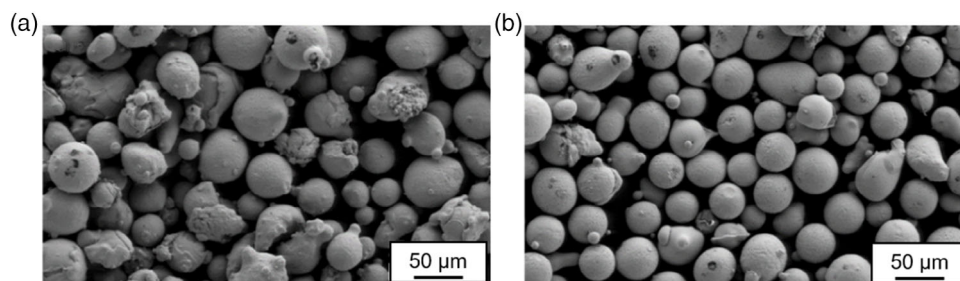

Figure 1. SEM micrographs of the powders: a) PMHS 6–5–3–8 and b) PMHS 7–7–7–11.

ADVANCED
SCIENCE NEWS
www.advancedsciencenews.com

steel
research
international

www.steel-research.de

Table 1. Chemical composition of the used powders, calculated composition of the mixed alloys and compositional range of the standard as mass percentages.

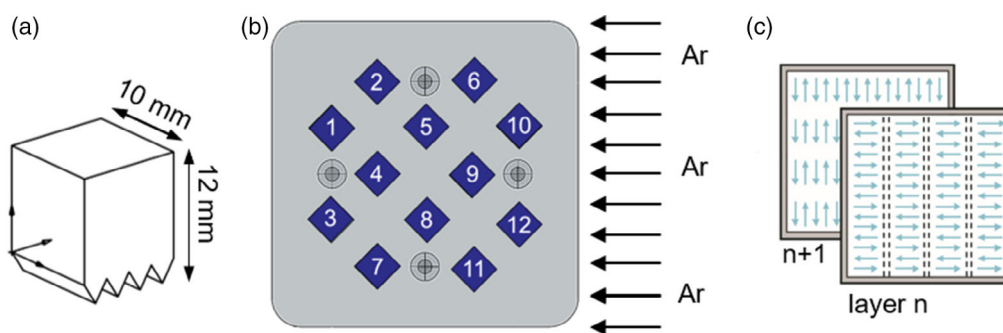|	C [%]	Cr [%]	Mo [%]	V [%]	W [%]	Co [%]
PMHS 5–5–3–8 (experimental)	1.33	4.2	4.6	2.8	6.7	8.7
PMHS 5–5–3–8 (standard)[24]	1.23–1.33	3.8–4.5	4.7–5.3	2.7–3.2	5.9–6.7	8.0–8.8
70:30 (calculated)	1.58	4.2	5.2	4.1	7.0	9.2
50:50 (calculated)	1.75	4.2	5.7	4.9	7.1	9.6
30:70 (calculated)	1.92	4.2	6.1	5.7	7.2	9.9
PMHS 7–7–7–11 (experimental)	2.17	4.2	6.7	7.0	7.4	10.4
PMHS 7–7–7–11 (standard)[24]	2.2–2.4	3.5–4.5	6.7–7.3	6.3–6.7	6.7–7.3	10.0–11.0

Figure 2. Set up of the build jobs a) specimen geometry, b) build plate arrangement, and c) scanning strategy.

Table 2. LPBF process parameter sets for all processed alloys.

Set	Exposure time [µs]	Point distance [µm]	Energy density [J mm^{-3}]
1	20	20	53
2	20	40	27
3	80	70	61
4	40	40	53
5	40	60	36
6	40	80	27
7	60	50	64
8	60	40	80
9	60	60	53
10	60	80	40
11	80	60	71
12	80	80	53

1 pixel µm^{-1} were used. The fraction between black and white areas was determined using Fiji-ImageJ software,[18] as pores appearing in black reduce the relative density.

Electron backscatter diffraction (EBSD) scans, energy dispersive X-ray spectroscopy (EDS) measurements, and backscatter electron images (BSE) were recorded with a Helios NanoLab DualBeam SEM (ThermoFisher Scientific, Hillsboro, USA)

and parameters were set to 15 kV and 2.8 nA. The step size of the EBSD measurement was set to 0.05 µm. The analysis of EBSD was carried out with TSL OIM Datacollection 7 and OIM Analysis 7 (EDAX, AMETEK, Berwyn, USA). For the evaluation, the phases austenite ($a = 3.65$ Å) and ferrite ($a = 2.87$ Å) were considered. Phase fractions were calculated, and orientation relationships of austenite and ferrite were determined.

A focus ion beam (FIB) lamella, kindly prepared and analyzed by GFE of RWTH Aachen, of PMHS 6–5–3–8 was extracted from a vertical cross section. The analyzed plane in the lamella therefore is perpendicular to the build direction. The lamella was cut by FIB in a FEI Strata 400 workstation and mounted on a copper grid. Imaging of the lamella was carried out in a transmission electron microscope Zeiss Libra200FE.

X-ray diffraction (XRD) was used for phase analysis and was carried out on a computer-controlled four-axis-two-circle diffractometer (former Seifert Analytical X-Ray, XRD Eigenmann GmbH, Schnaittach-Hormersdorf, Deutschland) with Cr Kα radiation at 40 kV and 40 mA. The intensity distribution was recorded in the range of $50° \leq 2\theta \leq 165°$ with a counting time of 10 s and a step size of 0.06°. To verify whether a texture is present, measurements were made at different tilts ($\psi = 0°$, $\psi = 45°$). In the case of random orientation, there is no difference between the measurements. A present texture affects the intensity of the reflection peak as crystallites are stronger or weaker in the reflection position.

2.5. Hardness Testing

Hardness (Vickers HV 10) was tested according to DIN EN ISO 6507.[19] The hardness indentations were placed over the height and width of the vertically cut cross sections of the specimens.

3. Results

3.1. Thermodynamic Calculations

Equilibrium calculations based on the theoretically calculated composition indicate the amount and the compositions of stabilized phases in the different alloys. Although the LPBF process is far from equilibrium, it allows a direct comparison of the analyzed alloys. The maximum expectable amount of carbides becomes apparent. From this, the variation of the LPBF process from the equilibrium becomes obvious. Further, the differences in the microstructure with different processing parameters is interpretable. The stable phase fractions of the base alloys and their mixtures in relation to the temperature are shown in **Figure 3**. **Table 3** shows an overview of the carbide content in thermodynamic equilibrium at solidus temperature.

At solidus temperature, the alloy PMHS 6–5–3–8 contains about 11% carbides. Theoretically, 3% are MC carbides and 8% M_6C carbides. From solidus to $\gamma \rightarrow \alpha$ transition temperature the M_6C carbide content increases. Carbide formation in turn leads to a reduction of carbide forming elements in the matrix, which influences the martensite start temperature.

Similarly, a microstructure consisting mainly of austenite, MC carbides, and M_6C carbides is stabilized in the alloy PMHS 7–7–7–11 above the A_3 temperature. The stabilized carbide content at solidus temperature consists of 11% MC and 9% M_6C carbides resulting in an overall carbide content of 20%. The theoretical carbide content is consequently approximately twice as high as that of PMHS 6–5–3–8, which results mainly from the higher MC carbide content.

Table 3. Overview of the carbide content at solidus temperature in thermodynamic equilibrium.

	PMHS 6–5–3–8	70:30	50:50	30:70	PMHS 7–7–7–11
Total carbide content [%]	11	15	17	18	20
MC content [%]	3	6	8	9	11
M_6C content [%]	8	9	9	9	9
MC/M_6C [-]	0.4	0.7	0.8	1	1.2

Processing mixtures of the powders of PMHS 6–5–3–8 and PMHS 7–7–7–11 offers the possibility to investigate intermediate composition stages. Increasing the PMHS 7–7–7–11 amount leads to an increased amount of stable MC carbides. At solidus temperature, the amount ranges from 6% in the 70:30 alloy, to 8% in the 50:50 alloy, and 9% in the 30:70 alloy. The amount of M_6C carbides remains quite stable within the analyzed window of alloying composition at 9%. With the overall increase in carbide content the amount of austenite is reduced accordingly. Evidently, the carbide content increases with increased content of PMHS 7–7–7–11 and the ratio of MC/M_6C increases simultaneously.

A phase diagram of compositions ranging from pure PMHS 6–5–3–8 to pure PMHS 7–7–7–11 is shown in Figure 3b. The abscissa of the phase diagram shows the change in the chemical composition as a linear function of the concentration of each alloying element in relation to the mixing ratio. This phase analysis allows a closer look at the influence of the change in alloying contents on the phase boundaries. With increasing PMHS 7-7-7-11 content the liquidus temperature (L) of the austenite (γ) is reduced, the precipitation temperature of the MC carbide is increased. As the liquidus temperature is reduced and the solidus temperature remains almost constant, the size of the solidification interval is reduced. The formation temperature of the M_6C carbide remains almost unchanged.

Scheil–Gulliver calculations allow an analysis of the solidification behavior of an alloy in case of a solidification-related segregation. The predicted solidification order differs from the
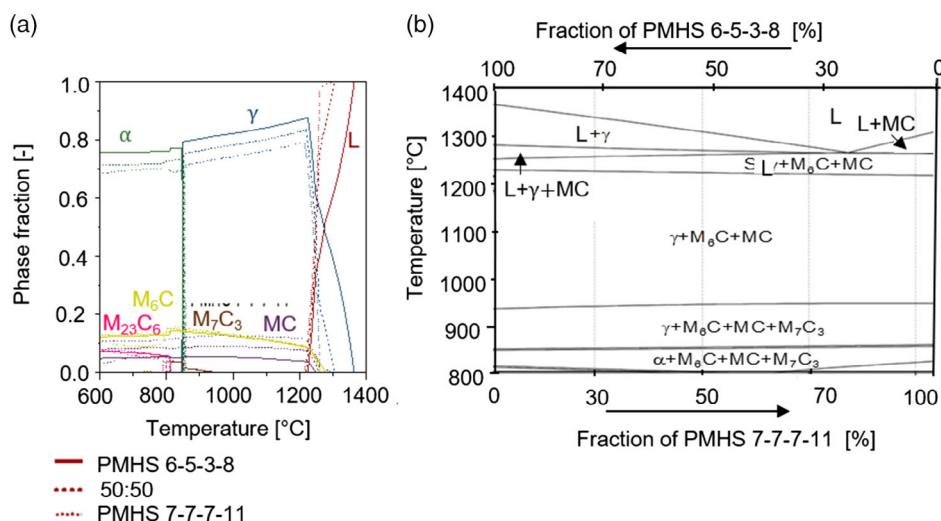

Figure 3. a) Theoretic behavior of the alloys in the thermodynamic equilibrium; b) Phase diagram plotted as a function of the chemical composition of increasing PMHS 7–7–7–11 content.
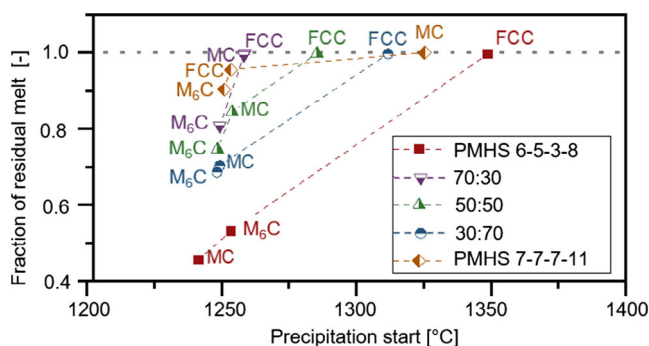
**ADVANCED
SCIENCE NEWS**

www.advancedsciencenews.com

**steel
research**
international

www.steel-research.de

Figure 4. Start of solidification of each phase in each alloy according to Scheil-Gulliver calculations.

solidification order in Figure 3. With the addition of PMHS 7–7–7–11, a shift in the order of carbide formation is predicted. Other than in pure PMHS 6–5–3–8, all alloys are expected to form MC carbides before the formation of M_6C carbides.

The starting temperature of crystallization of a phase in correlation to the fraction of residual melt is shown in **Figure 4** for all alloys. The liquidus temperature of PMHS 6–5–3–8 is 1349 °C. Below this temperature, the mentioned sole austenitic solidification is expected until M_6C carbide precipitation starts at a melt fraction of 53% and a temperature of 1252 °C, followed by MC precipitation at a melt fraction of 45% and a temperature of 1241 °C.

The solidification of PMHS 7–7–7–11 differs from PMHS 6–5–3–8. Initially, 4% MC carbides form from the melt starting at 1324 °C, before the austenite phase stabilizes at 1252 °C, resulting in a decrease in the austenite forming temperature of 97 K compared with PMHS 6–5–3–8. M_6C carbides form at a temperature only slightly below the austenitic solidification at 1249 °C. Strong solidification-induced segregation can additionally lead to the formation of M_7C_3 carbide at the end of solidification.

The alloys of mixed feedstocks (70:30; 50:50; and 30:70) initially solidify austenitic. As already seen in the phase diagram, with increasing PMHS 7–7–7–11 content, the liquidus temperature decreases. For the 70:30, 50:50, and 30:70 alloys, the liquidus temperatures are 1311, 1284, and 1258 °C, respectively. At the same time, carbide precipitation is predicted to start at higher residual melt contents compared with PMHS 6–5–3–8. This effect is more dominant in the formation of MC carbides than of the M_6C carbides. In the 70:30 alloy, the MC carbides theoretically start to form at 69% of residual melt. Within the 30:70 alloy, the MC carbide precipitation starts at 97% residual melt close to the liquidus temperature. The M_6C formation shifts from 66% residual melt to 78% with increasing PMHS 7–7–7–11 content from 30% to 70%.

Similar to the equilibrium phase diagram the Scheil–Gulliver calculations predict a smaller solidification interval with an increase in the PMHS 7–7–7–11 content up to 70%. The solidification intervals of PMHS 6–5–3–8, 70:30, 50:50, and 30:70 are 185, 153, 130, and 105 K, respectively.

3.2. LPBF Process

After LPBF, no cube was crack free. However, the difference between the alloys was clearly seen in the extent of the cracks.

Figure 5 shows a comparison of the crack tendency with increasing PMHS 7–7–7–11 content using parameter set 6 ($E_{V'} = 27\,\text{J}\,\text{mm}^{-3}$). The crack tendency visibly increases with increasing PMHS 7–7–7–11 content.

All cubes of alloy PMHS 6–5–3–8 contained fine cracks on the side edges. Two cubes built with the medium energy input showed additional cracks at one of the notches of the support structure.

During processing the alloy PMHS 7–7–7–11, partial detachment of the support structures from the build platform resulted in specimen protruding from the powder bed. To avoid damage to the recoater, all protruding cubes were removed from the exposure program during the process. After the process, all remaining cubes were heavily cracked. In addition to the detachments seen in Figure 5, vertical cracks starting from the notch of the tooth support structure and corkscrew-like cracks on the side of the cubes were observed.

After processing the powder mixtures, all specimen contained cracks. The cracks appeared on the side of the cubes, similar fine cracks to those of PMHS 6–5–3–8. The cracks within the cubes of the 50:50 alloy on the side edges were slightly more pronounced than the 70:30 alloy and partly moved corkscrew-like into a second crack plane. A more pronounced tendency to form vertical cracks is also seen in this alloy as one of the cubes also showed a vertical crack. All cubes of the 30:70 alloy showed several cracks at the edges. In some cubes, additionally to the horizontal cracks, tooth separations with vertical cracks parallel to the build-up direction were visible.

3.3. Porosity

The specimens of PMHS 6–5–3–8 show a low relative porosity in respect of the processing window. Exemplary images of three specimens are shown in **Figure 6**. The highest relative density was observed in specimen 4 ($E_V = 53\,\text{J}\,\text{mm}^{-3}$; Figure 6b) with $0.07 \pm 0.03\%$ porosity. A lower E_V of $27\,\text{J}\,\text{mm}^{-3}$ (specimen 2; Figure 6a) leads to the formation of small oval pores and a porosity of $0.16 \pm 0.05\%$. An increase in E_V results in the formation of larger circular pores, probably gas pores, as to be seen in specimen 8 ($Ev = 80\,\text{J}\,\text{mm}^{-3}$; Figure 6c) and a porosity of $0.97 \pm 0.3\%$. The 50:50 alloy showed the same tendency with values ranging from 0.25 ± 0.04 in specimen 2 ($E_V = 27\,\text{J}\,\text{mm}^{-3}$), 0.08 ± 0.02 in specimen 4 ($E_V = 53\,\text{J}\,\text{mm}^{-3}$), and $0.96 \pm 0.38\%$ in specimen 8 ($E_V = 80\,\text{J}\,\text{mm}^{-3}$). The porosity of PMHS 7–7–7–11 is not provided due to the mentioned high process instabilities and low reproducibility.

3.4. Microstructure

The microstructure of PMHS 6–5–3–8 is exemplarily shown in **Figure 7**. The melt pools can be distinguished easily from each other by the coarser appearing heat-affected zone (HAZ). Needle-like crystallites can be seen at the layer boundaries, some of which extend from one layer to the other. The influences of the energy input and thus the differences of the parameter set on the solidification type can be seen. Areas that have segregated due to dendritic solidification differ optically from the rest of the matrix. The segregation leads to an enrichment of carbide-
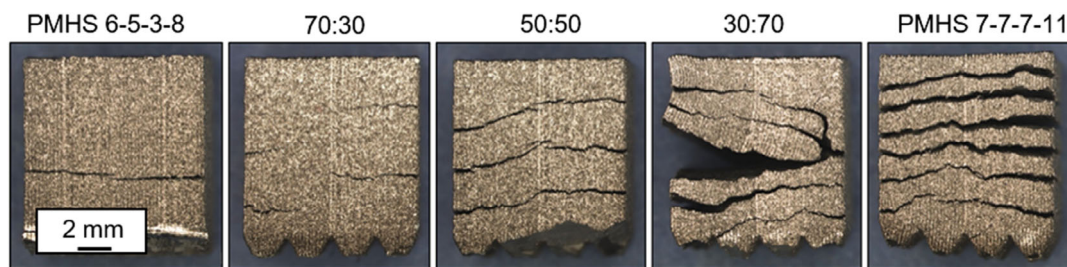
2100438 (5 of 14)

Figure 5. Crack formation tendency of set 6 ($E_V = 27\,\mathrm{J\,mm^{-3}}$) with increased alloying content of PMHS 7–7–7–11.
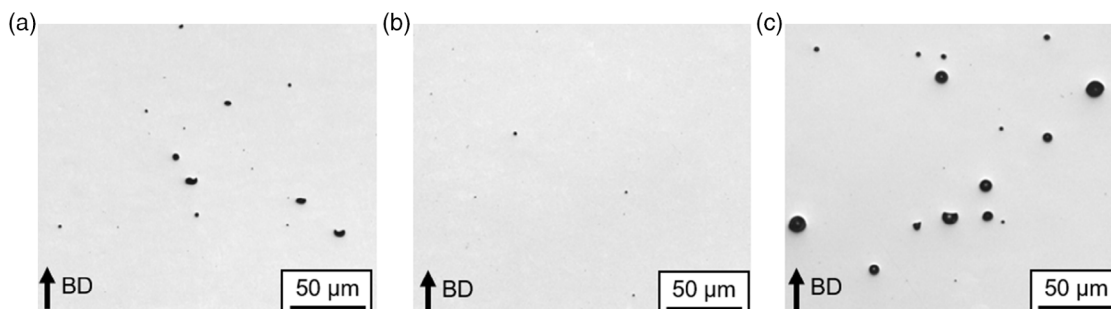
Figure 6. LOM images of unetched PMHS 6–5–3–8 of a) specimen 2 ($E_V = 27\,\mathrm{J\,mm^{-3}}$), b) specimen 4 ($E_V = 53\,\mathrm{J\,mm^{-3}}$), and c) specimen 8 ($E_V = 80\,\mathrm{J\,mm^{-3}}$), BD = building direction.
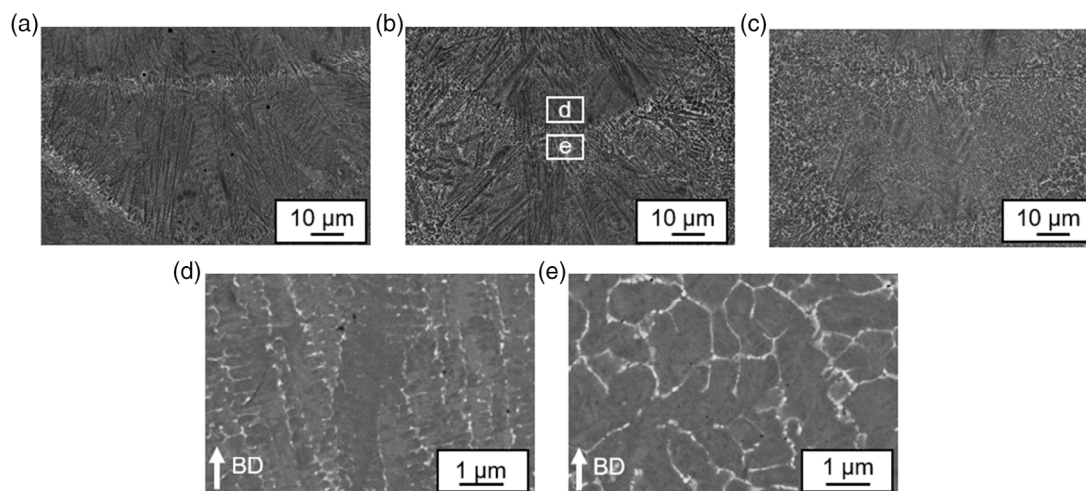
Figure 7. BSE images of melt pools in PMHS 6–5–3–8 a) specimen 2 ($E_V = 27\,\mathrm{J\,mm^{-3}}$), b) specimen 4 ($E_V = 53\,\mathrm{J\,mm^{-3}}$), c) specimen 8 ($E_V = 80\,\mathrm{J\,mm^{-3}}$); details from the d) bottom and e) the HAZ of PMHS 6–5–3–8 specimen 4 ($E_V = 53\,\mathrm{J\,mm^{-3}}$).

forming elements in the interdendritic region, appearing brighter than the dendrites, which leads to a local carbide formation. The proportion of columnar dendrites decreases with increasing energy input and the structure becomes more cellular.

The heat dissipation during melting heats up the underlying region to just below the melting point causing a coarsening of the structure within the HAZ (Figure 7e) as compared with the solidified dendrites (Figure 7b), shown exemplarily for specimen 4 ($E_V = 53\,\mathrm{J\,mm^{-3}}$).

BSE images of PMHS 7–7–7–11 specimen 8 ($E_V = 80\,\mathrm{J\,mm^{-13}}$), exemplarily shown in **Figure 8**a, show different solidification areas within the melt pool. Unlike in PMHS 6–5–3–8, no

needle-like dendrites can be seen in the melt pools. Only cellular dendritic solidified regions can be found in the entire specimen. A difference in cell size depending on their position can be observed. The cells at the bottom of a melt pool are small and become coarser with later solidification toward the top of a melt pool. The cells in the HAZ are also larger than those in the melt pool (Figure 8). Needle-shaped carbides (1) are visible at the cell boundaries, as well as angular and round carbides (2), mainly at the triple points. In addition, angular carbides can be found in the cell centers (3).

Inverse pole figure (IPF) maps in **Figure 9** of each phase from the collected EBSD data set allow further insights into the solidification behavior of the alloys. The martensite in PMHS 6–5–3–8
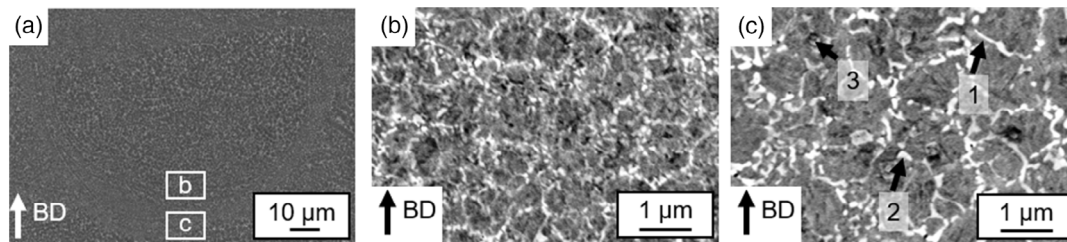
**ADVANCED
SCIENCE NEWS**

www.advancedsciencenews.com

**steel
research**
international

www.steel-research.de

Figure 8. BSE images of a) a melt pool of PMHS 7–7–7–11 specimen 8 ($E_V = 80$ J mm^{-3}) and details from the b) bottom of this melt pool and c) the HAZ; 1: needle shaped carbides and 2: angular carbides at cell boundaries 3: angular carbides in the cell center.
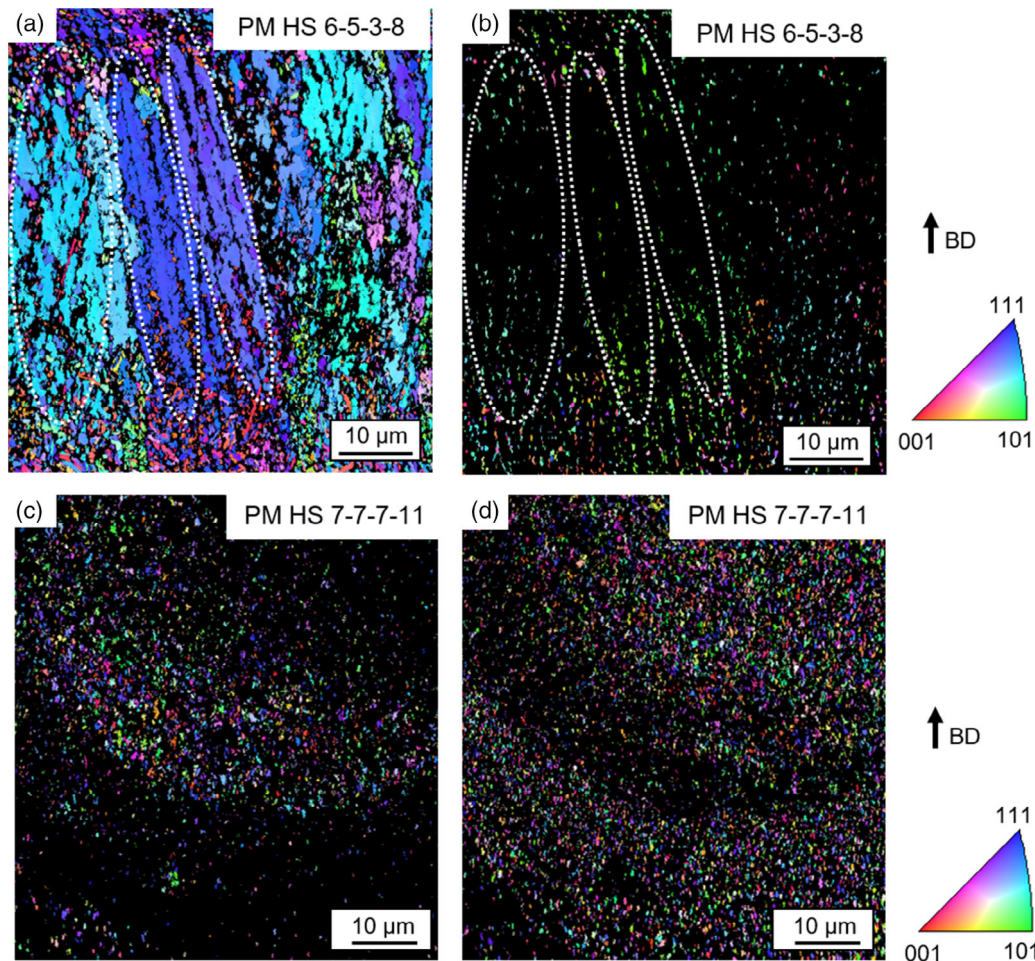

Figure 9. IPF maps of the a) ferrite and b) austenite phase in a PMHS 6–5–3–8 specimen 4 ($E_V = 53$ J mm^{-3}) melt pool and of c) ferrite and d) austenite phase of a melt pool in PMHS 7–7–7–11 specimen 8 ($E_V = 80$ J mm^{-3}).

(Figure 9a) shows elongated grains with the same orientation which are in building direction. The retained austenite (Figure 9b) within these regions shows an orientation relationship to the mentioned martensite. In regions where a cellular microstructure is apparent as observed in PMHS 7–7–7–11, a more random orientation in the martensite as well as the retained austenite becomes visible.

The microstructure of the 50:50 alloy changes significantly with the energy input. **Figure 10** shows the differences between the resulting microstructure caused by low (specimen 2

$[E_V = 27$ J mm$^{-3}]$), medium (specimen 4 $[E_V = 53$ J mm$^{-3}]$) and high energy input (specimen 8 $[E_V = 80$ J mm$^{-3}]$) of the 50:50 alloy. With lower energy input, the boundaries of the melt pool become easier distinguishable. In specimen 2 ($E_V = 27$ J mm^{-3}), the columnar dendrites start at the melt boundary and extend into the inner region until the solidification type changes into an equiaxial form. In specimen 8 ($E_V = 80$ J mm^{-3}), predominantly equiaxial dendrites are present.

A similar coarsening effect in the HAZ as in the two base alloys is observed in the powder mixtures. Exemplary for the finer
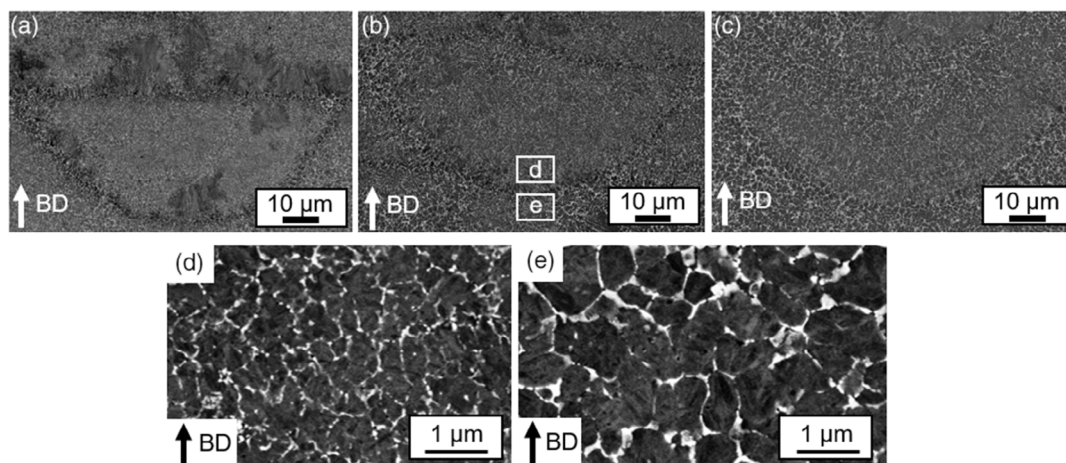
ADVANCED
SCIENCE NEWS
www.advancedsciencenews.com

steel
research
international
www.steel-research.de

Figure 10. BSE images of melt pools in a) specimen 2 ($E_V = 27 \, \text{J mm}^{-3}$), b) specimen 4 ($E_V = 53 \, \text{J mm}^{-3}$) and c) specimen 8 ($E_V = 80 \, \text{J mm}^{-3}$) of the 50:50 alloy; details from the d) bottom and e) the HAZ of the 50:50 alloy specimen 4 ($E_V = 53 \, \text{J mm}^{-3}$).

and coarser areas of the melting pool, BSE images of specimen 4 ($E_V = 53 \, \text{J mm}^{-3}$) are shown in Figure 10. At the melt pool boundary (Figure 10e) and overlap area, the equiaxial dendrite cells appear coarser than inside the melt pool with a more pronounced carbide network structure.

3.5. Phase Analysis

The normalized XRD reflection patterns of the specimen 2 ($E_V = 27 \, \text{J mm}^{-3}$), 4 ($E_V = 53 \, \text{J mm}^{-3}$), and 8 ($E_V = 80 \, \text{J mm}^{-3}$) of the alloy PMHS 6–5–3–8 and the 50:50 alloy are shown in **Figure 11**. The analysis of PMHS 7–7–7–11 specimen 8 ($E_V = 80 \, \text{J mm}^{-3}$) is included as well. Due to the described

difficulties in the LPBF processing of this alloy, the other specimens cannot be analyzed accordingly.

In a qualitative comparison of the measurement, the alloy PMHS 6–5–3–8 shows a decreasing retained austenite and an increased MC content with increased energy input. The measurements on specimen 2 ($E_V = 27 \, \text{J mm}^{-3}$), 4 ($E_V = 53 \, \text{J mm}^{-3}$) and 8 ($E_V = 80 \, \text{J mm}^{-3}$) of the 50:50 alloy show an identical trend. The lowest energy input (specimen 2 [$E_V = 27 \, \text{J mm}^{-3}$]) leads to the highest austenite content. A MC-reflex can be identified for all three specimens of the 50:50 alloy. The XRD pattern of alloy PMHS 7–7–7–11 (specimen 8 [$E_V = 80 \, \text{J mm}^{-3}$]) contains reflections of γ (austenite), α (ferrite/ martensite), and MC carbide (vanadium carbides). The MC reflexes are much more pronounced than in PMHS 6–5–3–8 and
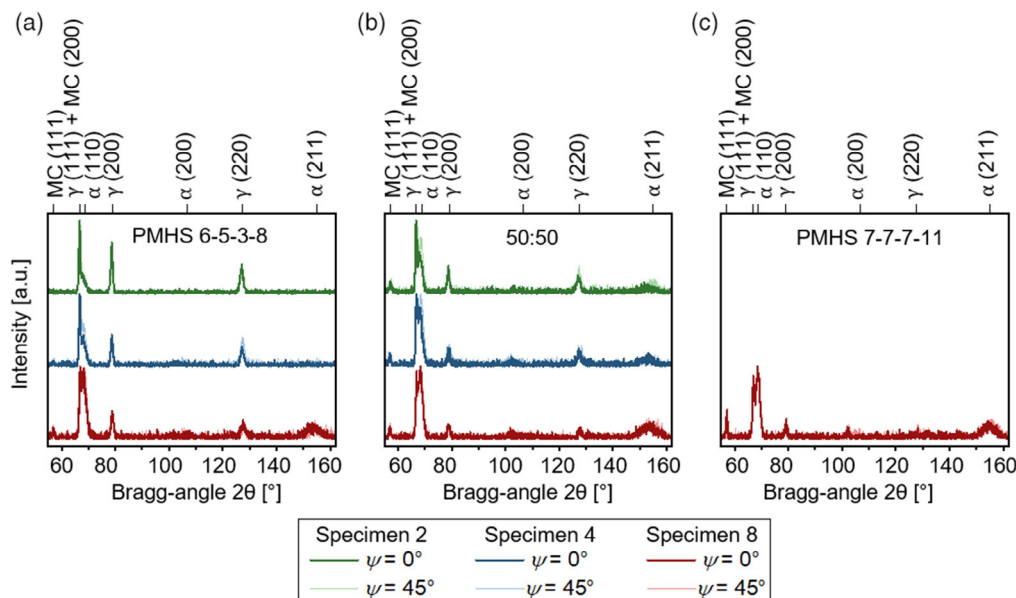

Figure 11. XRD measurements of ψ–0° and ψ–45° angles on specimen 2 ($E_V = 27 \, \text{J mm}^{-3}$), 4 ($E_V = 53 \, \text{J mm}^{-3}$), and 8 ($E_V = 80 \, \text{J mm}^{-3}$) on of PMHS 6–5–3–8 and the 50:50 alloy, and specimen 8 ($E_V = 80 \, \text{J mm}^{-3}$) of PMHS 7–7–7–11.
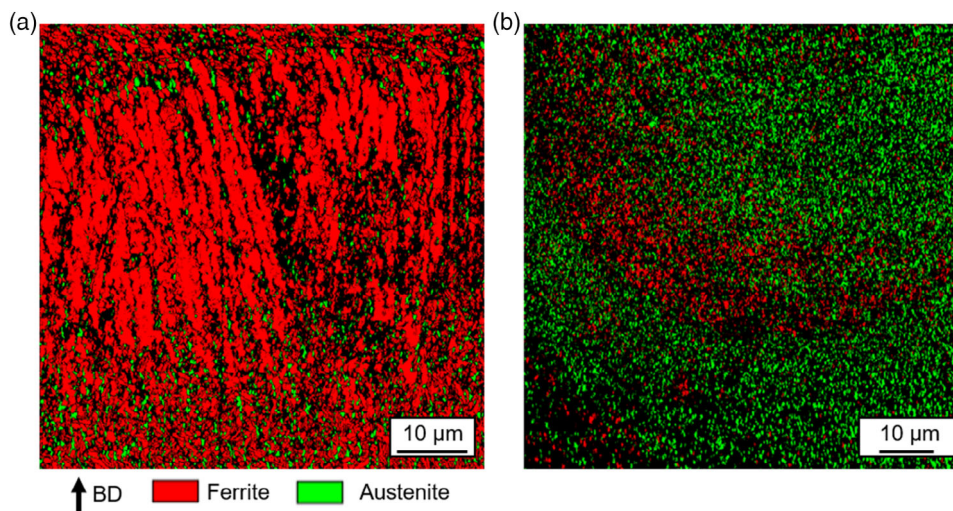
**ADVANCED
SCIENCE NEWS**

www.advancedsciencenews.com

**steel
research**
international

www.steel-research.de

Figure 12. EBSD phase mapping of a) PMHS 6–5–3–8 specimen 4 ($E_V = 53\,\mathrm{J\,mm^{-3}}$) and b) PMHS 7–7–7–11 specimen 8 ($E_V = 80\,\mathrm{J\,mm^{-3}}$).

the 50:50 alloy. In PMHS 7–7–7–11, the α-reflex (110) has a higher-measured intensity than the (111) γ-reflex suggesting a larger martensite content. The martensite content, therefore, increases with the energy input as well as with the PMHS 7–7–7–11 content. The course of specimen 8 ($E_V = 80\,\mathrm{J\,mm^{-3}}$) of PMHS 7–7–7–11 shows a more pronounced MC reflection compared to all other specimens.

The measurements with $\psi = 0°$ and $\psi = 45°$ in PMHS 6–5–3–8 show deviations from each other and indicate the presence of a certain texture. The deviation of the two measurements of different tilts becomes less with increasing energy input. An identical conclusion is valid for the 50:50 alloy. A quantification of the phases in all alloys was not possible due to this observed intensity dependence on the tilt angle.

EBSD measurements allow a phase analysis on a local level. **Figure 12**a shows the EBSD measurement of a specimen 4 ($E_V = 53\,\mathrm{J\,mm^{-3}}$) melt pool of PMHS 6–5–3–8. This melt pool mainly consists of martensite. In the interdendritic region of columnar dendrites austenite was detected, although the indexing rate in the interdendritic space is significantly lower than in the dendrites. More austenite was indexed in the cellular zone than in the dendritic region.

The indexing rate was lower for PMHS 7–7–7-11 (Figure 12b) for the EBSD measurement due to the significant higher and finely dispersed carbide content and the fine cellular structure. It is still apparent that the lower part of the melt pool contains a higher fraction of martensite than the later solidified top area. Both scans cannot be used for a phase quantification due to the described indexing difficulties in certain areas.

3.6. Carbides

The segregations in the interdendritic regions and the carbides are analyzed in more depth by EDS (**Figure 13**). Cr, Mo, V, and W contents are elevated in the interdendritic regions of PMHS 6–5–3–8, whereas Fe and Co concentrations are higher in the dendrites. Mo, Cr, and W are distributed on the cell edges as well

as on the triple points (1), whereas vanadium agglomerates mostly at triple points and less in the interdendritic space (2).

A cell structure has been created by the solidification-induced segregation in PMHS 7–7–7–11. Mo, Cr, V, and W accumulate at the cell boundaries (1) and carbides were precipitated in the enriched areas. The formation of a Mo–W–(Cr)-rich carbide leads to a local depletion of vanadium (3). V accumulates in the immediate surrounding of the carbide. The carbides precipitated inside the cells are rich in V and contain Mo, W, and Cr as well (2). Based on the element ratios of the carbide types known in the literature,[20] the V-rich carbides can be assigned to MC and the Mo- and W-rich carbides to M_2C or M_6C.

The element mappings of the transition from the lower part of the molten pool to the HAZ in the 50:50 alloy show that the elements Mo, Cr, W, and V accumulate more at the cell edges and the elements Fe and Co within the cells, which is similar to the alloy PMHS 6–5–3–8. In the HAZ, an increased content of V-rich carbides could be identified (1). The mark (2) shows a larger area where Fe is depleted and the carbide formers have accumulated. The bright carbides (3) seem to have formed more strongly as observed in PMHS 6–5–3–8.

Due to the fine nature of the formed carbides a characterization only becomes possible with even higher resolutions. EDS spectra were recorded at a FIB lamella. Measuring spots are shown in the high-angle annular dark field (HAADF) image of **Figure 14**. The two carbides (1, 3) appearing bright in the HAADF image show a higher proportion of molybdenum and tungsten as well as vanadium and chromium than the matrix (4). The intensities of the carbide forming elements are stronger in the bright carbide located at the corner point (3). A round morphology with a diameter of about 30 nm (2) was identified immediately next to the medium bright rod-shaped carbide (1). The measurement there (2) showed a slightly higher vanadium and chromium content compared with the matrix. The small difference to the matrix can be explained by the small size of the structure through which the underlying matrix is included in the measurement. The different intensities of the copper reflexes are attributed to an interference with the Cu-grid on which the lamella is mounted.
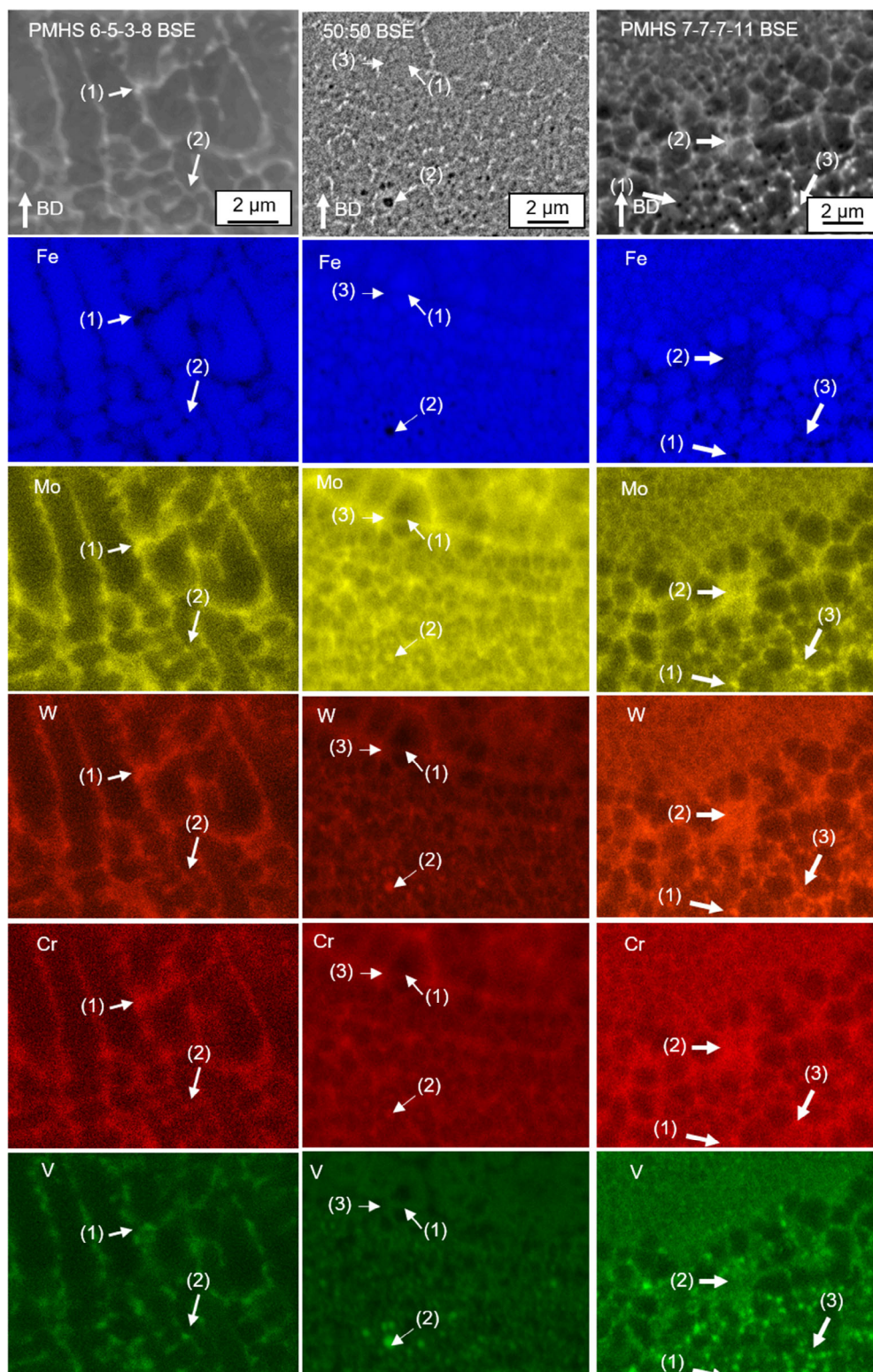
**ADVANCED
SCIENCE NEWS**

www.advancedsciencenews.com

**steel
research**
international

www.steel-research.de

Figure 13. EDS mappings of PMHS 6–5–3–8 specimen 4 ($E_V = 53$ J mm^{-3}), 50:50 alloy specimen 4 ($E_V = 53$ J mm^{-3}), and PMHS 7–7–7–11 specimen 8 ($E_V = 80$ J mm^{-3}) in the transition area of HAZ to melt pool boundary.

**ADVANCED
SCIENCE NEWS**

www.advancedsciencenews.com

**steel
research**
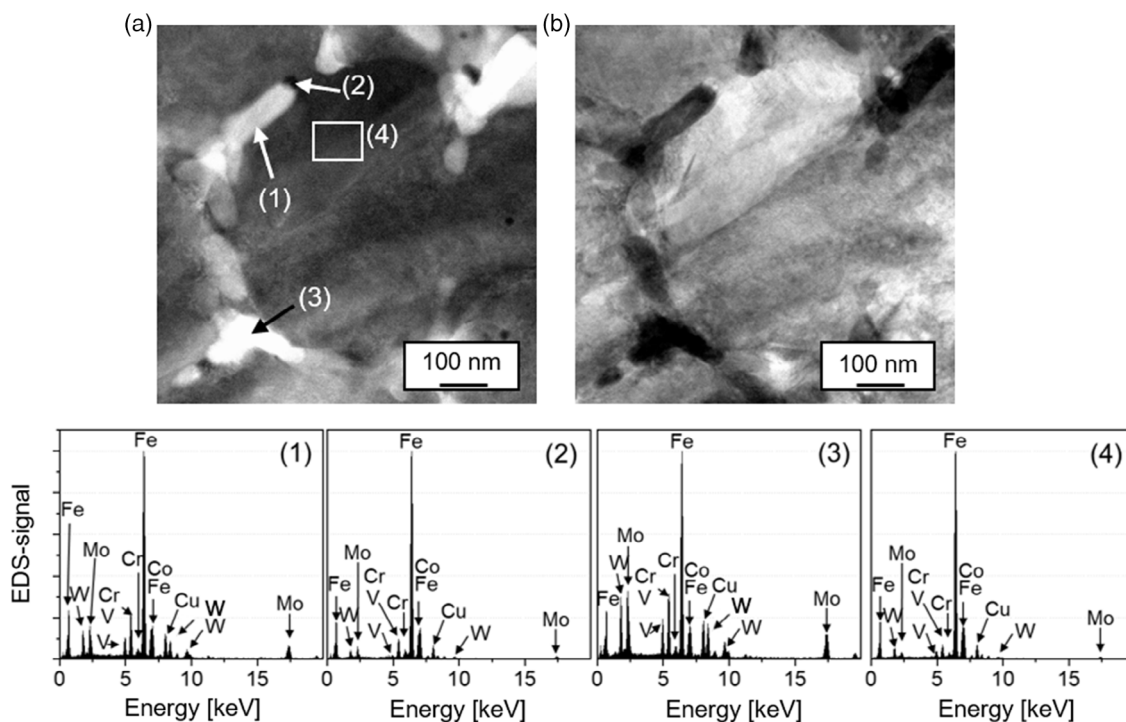international

www.steel-research.de

Figure 14. a) HAADF and b) bright field (BF) images of an area in a PMHS 6–5–3–8 FIB lamella and spectra of the corresponding EDS point measurements.

Table 4. Measured hardness values of specimen 2 ($E_V = 27\,J\,mm^{-3}$), 4 ($E_V = 53\,J\,mm^{-3}$) and 8 ($E_V = 80\,J\,mm^{-3}$) of PMHS 6–5–3–8, 50:50 and PMHS 7–7–7–11.

Specimen (E_V)	Hardness [HV10]	
	PMHS 6–5–3–8	50:50
2 ($E_V = 27\,J\,mm^{-3}$),	571 ± 4	700 ± 9
4 ($E_V = 53\,J\,mm^{-3}$)	696 ± 16	834 ± 15
8 ($E_V = 80\,J\,mm^{-3}$)	836 ± 15	920 ± 23

3.7. Hardness Testing

In **Table 4**, the measured hardness values of specimen 2 ($E_V = 27\,J\,mm^{-3}$), 4 ($E_V = 53\,J\,mm^{-3}$), and 8 ($E_V = 80\,J\,mm^{-3}$) of PMHS 6–5–3–8 and 50:50 are listed. The measured hardness of the alloy PMHS 6–5–3–8 increases with increasing energy density. The hardness is between 571 HV10 and 836 HV10, the difference between the minimum and maximum value is thus 265 HV10. The hardness of specimen 2 ($E_V = 27\,J\,mm^{-3}$), specimen 4 ($E_V = 53\,J\,mm^{-3}$) and specimen 8 ($E_V = 80\,J\,mm^{-3}$) of the 50:50 alloy shows a similar trend with hardness' of 700 ± 9, 834 ± 15, and 920 ± 23 HV10, respectively, resulting in a hardness difference of 120 HV10 between the lowest and the highest energy input. The hardness of PMHS 7–7–7–11 cannot be provided due to processing difficulties and the high crack density.

4. Discussion

4.1. Thermodynamic Calculations

The increase in carbide content by increasing PMHS 7–7–7–11 content in thermodynamic equilibrium is solely due to the increased amount of stabilized MC carbides. The main difference in the alloying content relevant for carbide formation is the amount of carbon, in combination with an increased Mo content of 4.6 to 7.0%; V content from 3.0 to 6.6% and W from 6.3 to 7.0%. The enhanced affinity of V for carbide formation compared with Mo and W leads to the increase in MC carbides and the comparably stable amount of M_6C carbides.

The comparison of the alloys in terms of their theoretical solidification behavior showed that the starting temperature of carbide precipitation is barely changing until the alloying content of the 30:70 alloy. The M_6C carbide precipitation starts at the same temperatures and the precipitation temperature of MC carbides shows only a small increase. A significant increase in the MC carbide precipitation starting temperatures can be observed between the 30:70 alloy and the alloy PMHS 7–7–7–11. However, the austenite formation temperature is highly dependent on the alloying content as the liquidus temperature decreases strongly. The decreasing liquidus temperature and the nearly unchanged carbide precipitation starting temperature explain the carbide precipitation at increasing residual melt contents with increasing PMHS 7–7–7–11 content.

4.2. LPBF Processability

The side cracks are most likely initiated by tensile stresses parallel to the build-up direction of the specimen. The surface roughness caused by the layer-by-layer structure can act as a crack-initiating notch. The occurrence of vertical cracks can be explained by the notch effect of the tooth-like supporting structures. A vertical crack always occurs in combination with a horizontal crack, which leads to a local detachment of the cube from the building plate or support structure. The melting of a layer induces stresses in the underlying layers, leading to stresses that in case of lower yield strength at elevated temperatures can lead to plastic deformation. The crack grows with the height of the part, and the plastic deformation due to local thermal cycling leads to a visible curvature of the surface; in extreme cases leading to the necessary removal from the further build-up during the process as for PMHS 7–7–7–11. As the process parameters, such as laser power, scanning speed, and hatch strategy, remain unchanged, the change in chemical composition causes the decrease in resistance to stress-induced cracking and the resulting deformation. The increasing carbide content within the microstructure forming fine networks lead to the decreases cracking resistance, similar to carbide networks in cast tool steels.[4]

4.3. Porosity

The observed pores in the PMHS 6–5–3–8 and the 50:50 alloy are mostly spherical gas pores that become larger in size with increasing energy input. Gas pores are mainly attributed to a slightly too large energy input toward the higher end of the parameter window. The pores observed in the low energy input specimen are most likely due to an instable melt pool.[21] As the measured porosity in 50:50 and PMHS 6–5–3–8 samples is almost identical with respect to the processing parameters, it is independent from the alloying content in this compositional range. The porosity is known to be dependent on the viscosity of the liquid phase. A low viscosity leads to a better wetting behavior and results in a lower porosity.[22] This effect is highly interesting as carbide precipitation occurs at different residual melt fractions, influencing the viscosity of the melt without influencing the porosity to a relevant amount.

4.4. Microstructure

A shift from mainly columnar dendritic solidification in PMHS 6–5–3–8 toward equiaxed dendritic solidification in PMHS 7–7–7–11 is observed with increasing alloying content. This effect can also be seen in the 50:50 alloy and seems to be supported by certain process parameters. The increased contents of C, Mo, W, and V lead to the earlier precipitation of MC carbides in the melt, enlarging the nucleation sites for equiaxed dendritic solidification and thus increasing its proportion in the overall solidification. The growth of the individual grains occurs independently of each other and is therefore a possible explanation for the random grain orientation. At the same time, the solidification morphology is highly influenced by the portion of carbides. With a high portion of primary carbides in the melt of PMHS 7–7–7–11, with carbide precipitation starting theoretically 72 K above austenite formation, a large number of nucleation sites is available, limiting the space between the solidifying grains and leading to a fine-grained microstructure.

In the 50:50 alloy, a low E_V leads to the formation of relatively fine directional solidified dendrites whereas the portion of equiaxed dendrites increases with increasing E_V. The dependency of the solidification morphology on the LPBF parameters as observed in the 50:50 alloy is attributed to the following: By decreasing the scan speed, the solidification rate is decreased and consequently the solidification morphology is influenced. As the energy input increases, the structure becomes coarser, the austenite content decreases, and the hardness increases. In specimen 2 ($E_V = 27\,J\,mm^{-3}$), the columnar dendrites grow starts from the melt pool boundary. Slower solidification leads to a pronounced growth of the available dendrites leading to a coarser structure compared with fast solidification. The underlying layer forms the nucleus for dendrite growth. In competition, there are heterogeneous nuclei in the interior of the melt pool, on which radial crystallization takes place. The columnar dendrites grow towards the interior of the molten bath until they are hindered from further growth by the encounter with radially grown grains. At lower scanning speeds and thus higher energy input, the cellular appearance dominates, and directional solidification is almost completely suppressed. The higher heat input could additionally result in an increase in the number of favorable nucleation sites in the melt pool. The reason for this can be the break-off of dendrite tips or partially solidified grains caused by convection. The fragments are transported into the melt pool center where they act as a nuclei.[6–10]

The observed coarsening in the HAZ of all alloys is caused by the heat dissipated from the melted layer above. This coarsening effect depends on the amount of energy deposited and the coarsening increases with higher energy inputs. The increased diffusion activity and the partial melting of the eutectic carbides probably lead to a coarsening of the cell structure and the renewed precipitation of the visible carbide network at the cell boundaries. This measured sensitivity of the material to changing process conditions bears the risk of creating highly pronounced property gradients, e.g., when processing complex geometries.

The influence of the constitutional supercooling on the transition of the solidification type caused by the powder mixture cannot be clearly evaluated. Collins et al.[23] suggested increasing the melting range as a possibility to influence the solidification mode. This should contribute to the transition from columnar to equiaxial solidification and thus to the reduction of textures. The observed solidification morphologies are opposite to this. Except for PMHS 7–7–7–11, the solidification range is reduced in the powder mixtures, but the microstructure tends toward equiaxial–dendritic solidification. Presumably, this effect is superimposed by the early formation of the thermodynamically stable MC carbide during solidification. A positive effect of equiaxed solidification is the expected reduced texture. Except for some materials, the texture cannot be dissolved by recrystallization in a subsequent heat treatment due to the lack of driving force.[23] Therefore, an avoided texture can be advantageous regarding the isotropy of the properties. The positive effect of the reduced texture is negated by the obvious negative effect of a stronger cracking tendency. The transition to a fine cellular structure increases the number of grain boundaries. The carbides located at the boundaries tend to have a fracture resistance-reducing effect, especially as the carbides form

**ADVANCED
SCIENCE NEWS**

www.advancedsciencenews.com

**steel
research**
international

www.steel-research.de

networks. In the HAZ, coarser carbides are present together with a martensitic matrix. In combination with a complex internal stress profile, this might lead to a stronger crack tendency in this area.

4.5. Phase Analysis

The XRD measurements confirmed higher contents of martensite in PMHS 6–5–3–8 with increasing E_V. Lower cooling rates and the higher heat input favor the transformation of austenite to martensite, due to MC carbide formation and the resulting depletion of the austenite with C. Large cooling rates lead to an enriched interdendritic austenite area suppressing the martensite start temperature below room temperature. In addition, the VC reflex is more pronounced in specimen 8 ($E_V = 80\,\mathrm{J\,mm^{-3}}$), suggesting a C-depleted austenite and thus a higher martensite start temperature. The different content of retained austenite and carbides in the specimen may have contributed to the significant differences in hardness measured. The XRD and hardness measurements show that the alloy PMHS 6–5–3–8 reacts particularly sensitive to changing process conditions within the selected parameter range. The higher content of carbides is proposed to be dominant effect on the hardness changes when changing the alloys composition and increasing the content of carbide forming elements. The visible difference between the XRD measurements with $\psi = 0°$ and $\psi = 45°$ and the correlated anisotropy tends to decrease with increasing energy input. This could be related to the decrease in columnar dendritic solidification in the 50:50 alloy shown in Figure 10. This observation is in good agreement with the low observed anisotropy and the random oriented grains in PMHS 7–7–7–11.

The orientations of martensite and retained austenite of PMHS 6–5–3–8 in Figure 9 show grain growth over the entire melt pool. The initially austenitic-solidified grain transforms to martensite and residual austenite remains in the interdendritic region due to segregation-induced stability of the austenite. Segregations are also observed toward the top of melt pool of PMHS 7–7–7–11 being in good agreement with higher fractions of retained austenite in this region.

An interpretation of the EBSD results should be taken carefully as the indexing rates were comparably low. The low indexing rates can be explained by too much lattice distortion and carbide formation in the interdendritic areas. Information about the austenite to martensite ratio is not to be drawn from the phase mappings. Fine distribution of a phase and large distortion can lead to a significant underestimation of one phase compared with the other.

4.6. Carbides

All alloys from this study show similar carbide precipitation behavior. V-rich carbides, presumably MC, as well as carbides enriched in Mo and W, presumably M_6C, are observed in the microstructure. Due to their fine dispersion in the matrix and their partially difficult distinction from partially enriched matrix phase a quantification, even in a FIB lamella, is very difficult. The structure of the carbide network is closely related to the solidification structure of the primary austenite. Whereas in PMHS 6–5–3–8, no carbides were observed within the dendrites PMHS 7–7–7–11 showed V-rich carbides within solidified austenite grains. With regards to the solidification behavior, the carbides

occurrence inside solidified austenite grains and their composition, these carbides are most likely MC carbides. The carbides on the cell boundaries however result from solidification segregation and enrichment of the residual melt in carbide forming elements and thus form eutectic carbides toward the end of the solidification. Considering the result of the Scheil–Gulliver solidification simulation, the formation of M_6C and MC carbides is likely. This type of carbides is observed in all alloys in the interdendritic regions, appearing bright in the BSE images. Considering the very fast solidification in the LPBF process, metastable phases could form as well. Expected M_6C carbides could precipitate in the metastable M_2C form and transform to M_6C carbides in a later postprocessing heat treatment.

A direct correlation between carbide network and crack formation could not be drawn from the observations. Crack formation is a product of many factors that influence each other. However, the characteristics of the carbide network are a relevant factor influencing crack formation. PMHS 7–7–7–11 theoretically has the highest carbide content of the investigated materials and showed poor processability within the selected process window as all cubes were heavily cracked.

5. Conclusion

In this study, two standard high-speed steels PMHS 6–5–3–8 and PM 7–7–7–11 as well as three powder mixtures thereof were processed by LPBF and their microstructure and phase formation were analyzed in detail. Thermodynamic equilibrium and solidification calculations are used to further understand the alloys behavior in the LPBF process. The following conclusions are drawn from the investigations: 1) In the used parameter window, PMHS 6–5–3–8 shows a crack formation tendency when being processed by LPBF. 2) PMHS 6–5–3–8 shows directional dendritic solidification with a pronounced texture. The hardness reached is sufficient for high-speed steel. 3) The microstructure of the 50:50 alloy shows neglectable inhomogeneity of porosity and phase fractions within the specimen, proving good processability of powder mixtures by LPBF when the powder particles have similar morphologies and densities. 4) Theoretically, predicted by ThermoCalc, an increase in the PMHS 7–7–7–11 content leads to a larger amount of precipitated MC carbides in the equilibrium state, whereas the M_2C and M_6C carbide content is fairly independent of the composition. 5) Increasing the PMHS 7–7–7–11 content up to 70% leads to a smaller solidification temperature range as liquidus temperature is decreased. 6) With increasing PMHS 7–7–7–11, the crack susceptibility of the alloys in LPBF becomes more pronounced. 7) An increased content of PMHS 7–7–7–11 leads to a shift from columnar dendritic solidification toward equiaxed, radial solidification. This effect occurs most likely due to the presence of primary MC carbides in the melt pool acting as solidification nuclei. 8) The solidification microstructure is furthermore dependent on the LPBF processing parameters. Large energy inputs lead toward a more equiaxed solidification. 9) Larger amounts of equiaxial solidified grains reduce the anisotropy of the microstructure in the alloys. 10) Eutectic carbides form in the interdendritic regions precipitating from solidification segregations.

2100438 (13 of 14)

[1] S. Kumar, in *Comprehensive Materials Processing*, Elsevier, Amsterdam **2014**, pp. 93–134.

[2] D. Herzog, V. Seyda, E. Wycisk, C. Emmelmann, *Acta Mater.* **2016**, *117*, 371.

[3] K. Kempen, et al., in *Solid Freeform Fabrication Symposium Proc.*

[4] P. Beiss, in *ASM Handbook*, Vol. *7*, pp. 489–537.

[5] a) J. Saewe, N. Carstensen, P. Kürnsteiner, E. A. Jägle, J. H. Schleifenbaum, *Addit. Manuf.* **2021**, *46*, 102125; b) J. Kunz, J. Saewe, S. Herzog, A. Kaletsch, J. H. Schleifenbaum, C. Broeckmann, *Steel Res. Int.* **2020**, 1900562; c) J. Saewe, C. Gayer, A. Vogelpoth, J. Kunz, C. Broeckmann, J. H. Schleifenbaum, in Metal Additive Manufacturing Conf.

[6] J. Sander, J. Hufenbach, L. Giebeler, H. Wendrock, U. Kühn, J. Eckert, *Mater. Des.* **2016**, *89*, 335.

[7] F. Kochta, A. Gebert, U. Kühn, S. Oswald, T. Gemming, C. Leyens, J. K. Hufenbach, *J. Alloys Compd.* **2021**, *867*, 158887.

[8] a) M. L. Koehler, J. Kunz, S. Herzog, A. Kaletsch, C. Broeckmann, *Mater. Sci. Eng., A* **2020**, 140432; b) P. G. E. Jerrard, L. Hao, K. E. Evans, *Proc. Inst. Mech. Eng., Part B: J. Eng. Manuf.* **2009**, *223*, 1409; c) A. Aversa, G. Marchese, D. Manfredi, M. Lorusso, F. Calignano, S. Biamino, M. Lombardi, P. Fino, M. Pavese, *Metals* **2018**, *8*, 300.

[9] S. Kou, *Welding Metallurgy*, Wiley-Interscience, Hoboken, N.J **2010**.

[10] C. T. Kwok, F. T. Cheng, H. C. Man, *Surf. Coat. Technol.* **2007**, *202*, 336.

[11] K. Geenen, A. Röttger, F. Feld, W. Theisen, *Addit. Manuf.* **2019**, *28*, 585.

[12] E.-S. Lee, W.-J. Park, J. Y. Jung, S. Ahn, *Metall. Mater. Trans. A* **1998**, *29*, 1395.

[13] G. Tang, F. Xu, G. Fan, X. Ma, L. Wang, *Nucl. Instrum. Methods Phys. Res. Sect. B* **2012**, *288*, 1.

[14] K. C. Hwang, S. Lee, H. C. Lee, *Mater. Sci. Eng., A* **1998**, *254*, 282.

[15] M. Wegst, C. W. Wegst, *Stahlschlüssel*, Marbach am Neckar **2019**.

[16] DIN EN ISO 3923-1 Metallpulver- Ermittlung der Fülldichte: Teil 1: Trichterverfahren.

[17] J.-O. Andersson, T. Helander, L. Höglund, P. Shi, B. Sundman, *Calphad* **2002**, *26*, 273.

[18] J. Schindelin, I. Arganda-Carreras, E. Frise, V. Kaynig, M. Longair, T. Pietzsch, S. Preibisch, C. Rueden, S. Saalfeld, B. Schmid, J.-Y. Tinevez, D. J. White, V. Hartenstein, K. Eliceiri, P. Tomancak, A. Cardona, *Nat. Methods* **2012**, *9*, 676.

[19] DIN EN ISO 6507-1:2016 Metallische Werkstoffe - Härteprüfung nach Vickers: Teil 1: Prüfverfahren.

[20] A.-M. Elrakayby, B. Mills, *J. Mater. Sci. Lett.* **1986**, *5*, 332.

[21] J. P. Oliveira, A. D. LaLonde, J. Ma, *Mater. Des.* **2020**, *193*, 108762.

[22] A. Simchi, H. Asgharzadeh, *Mater. Sci. Technol.* **2004**, *20*, 1462.

[23] P. C. Collins, D. A. Brice, P. Samimi, I. Ghamarian, H. L. Fraser, *Annu. Rev. Mater. Res.* **2016**, *46*, 63.

[24] C. W. Wegst, M. Wegst, *Stahlschlüssel*, Marbach am Neckar **2019**.